

## Critical enhancement of thermoelectric properties with doping-induced second-order ferroelectric transition in BaTiO<sub>3</sub>

Haifeng Luo  and Bin Xu \*

*Institute of Theoretical and Applied Physics, Jiangsu Key Laboratory of Thin Films, School of Physical Science and Technology, Soochow University, Suzhou 215006, China*



(Received 6 December 2023; accepted 1 February 2024; published 26 February 2024)

Doping a conventional ferroelectric insulator can yield intriguing changes in its electronic transport properties, in particular when a polar-to-nonpolar transition occurs. In this work, we study the effect of electron doping on the resistivity and Seebeck coefficient of the prototypical ferroelectric BaTiO<sub>3</sub>, which undergoes a tetragonal-to-cubic second-order phase transition at a critical doping concentration. The transport properties are computed using two first-principles methods: (1) The constant relaxation time approximation and (2) the fully *ab initio* variational approach considering explicitly electron-phonon coupling. We show that the doping effect on the transport properties is manifold, via upshift of the Fermi level, variation of the band structure (tetragonal towards cubic), and phonon softening around the transition point, which causes nonmonotonic changes of the resistivity and Seebeck coefficient, especially the anomalies close to the transition point. Results of the two methods are compared, and the effect of temperature is also discussed.

DOI: [10.1103/PhysRevB.109.054114](https://doi.org/10.1103/PhysRevB.109.054114)

### I. INTRODUCTION

Polar metal is a concept put forth by Anderson and Blount in 1965 [1] in which metallicity coexists with polar atomic displacements that break the centrosymmetry. Since polar metals share many similarities with good thermoelectric materials, such as the level of carrier concentration, good electric conductivity, and large Seebeck coefficient, they have good potentials for thermoelectric applications [2,3]. In particular, doping a conventional ferroelectric material constitutes an extrinsic approach to generating a polar metal, and this allows fine-tuning of the thermoelectric properties by controlling the doping concentration.

Electrical transport properties, such as the resistivity and Seebeck coefficient, are fundamental attributes of a metal that can be conveniently measured. Besides their relevance to many important applications, e.g., providing desirable conductivity (or resistivity) and waste-heat recovery, they may exhibit fascinating characteristic changes and involve rich physics when a structural phase transition occurs. For instance, a first-order structural transformation is usually accompanied by abrupt changes of the transport properties, e.g., in Co [4,5], CaFe<sub>2</sub>As<sub>2</sub> [6], Fe<sub>1.11</sub>Te [7], and Cu<sub>2</sub>Se [8], whereas for second-order structural transitions the change in transport properties can be more intriguing, e.g., being continuous in RCo<sub>2</sub> compounds (*R*=rare earth) [9] or showing anomalies in Sr<sub>3</sub>Ir<sub>4</sub>Sn<sub>13</sub> [10], Sr<sub>3</sub>Rh<sub>4</sub>Sn<sub>13</sub> [11], Ce<sub>3</sub>Rh<sub>4</sub>Sn<sub>13</sub> [12], and IV–VI compounds likely due to scattering of electrons with softening phonon modes [13]. In particular, among these examples, very small structural variation across the phase transition can often result in significant changes of the

transport properties, such that these measurements can be used to characterize the phase transition.

BaTiO<sub>3</sub> is the prototype of perovskite ferroelectric oxide, and its thermoelectric transport coefficients were theoretically studied with electron doping in the high-symmetry cubic phase (*C* phase, space group: *Pm3m*) [14]. However, the cubic phase is only stable at high temperature or with high electron doping. The most stable structure of BaTiO<sub>3</sub> around room temperature is the polar tetragonal phase (*T* phase, space group: *P4mm*), and upon heating the ferroelectric *T* phase transits into the paraelectric *C* phase at 403 K [15], which is of first order in nature. With electron doping, e.g., via oxygen vacancies as in of BaTiO<sub>3-δ</sub>, it has been demonstrated that the *T* phase can be retained upon electron doping below a critical concentration, whereas above a doping level of approximately  $\sim 10^{21} \text{ cm}^{-3}$  the *T* phase transforms into the nonpolar *C* phase, according to several theoretical [16–19] and experimental studies [20,21]. The tetragonal-to-cubic (*T*-to-*C*) transition temperature strongly decreases with doping concentration [20,22]. In doped samples, the measured resistivity as a function of temperature was found to show a small hysteresis loop near the phase transition temperature [20], while the Seebeck coefficient varies without apparent anomaly across the transition point [23]. However, it is interesting to note that in contrast to the temperature-induced *T*-to-*C* transition, the same transition induced by electron doping is predicted to be a second-order transition by density-functional theory (DFT) [16–19], associated with continuous variations of the structural parameters. And, more interestingly, soft polar phonons and strong electron-phonon coupling were found around the critical concentration according to first-principles calculations [19]. It is thereupon a natural question whether the strong coupling between the electrons and the soft phonons can lead to anomalies in the transport properties near the doping-induced *T*-to-*C* transition, which so far has not been explored yet.

\*Corresponding author: [binxu19@suda.edu.cn](mailto:binxu19@suda.edu.cn)

In this paper, we investigate the effect of electron doping on the electronic transport properties, including resistivity and Seebeck coefficient, using two computational approaches within the framework of Boltzmann's transport theory: (1) The widely adopted constant relaxation time approximation (CRTA) and (2) the variational approach (VA) based on fully *ab initio* electron-phonon coupling. Their variations as a function of doping concentration are discussed in detail, and a particular focus is given to the critical behavior around the transition point, where the two methods yield distinctly different results, i.e., no anomaly from CRTA and a critical enhancement from VA. The temperature effect on the transport properties is also reported.

The remainder of the paper is organized as follows. A description of the computational methods is provided in Sec. II. Section III reports and discusses the evolution of structure and band structure upon electron doping, the transport properties calculated with the CRTA and VA methods, and the effect of temperature at selected doping concentrations with VA. Finally, we summarize the study in Sec. IV.

## II. COMPUTATIONAL DETAILS

All the first-principles calculations were performed using density-functional theory and density-functional perturbation theory (DFPT), as implemented in the ABINIT package [24,25]. We used the Teter "extended norm-conserving" pseudopotentials with local-density approximation (LDA) as the exchange and correlation functionals, which can yield the doping-induced *T*-to-*C* phase transition. Note that we numerically found that such transition is absent with other LDA pseudopotentials such as Troullier-Martins, Fritz-Haber-Institute, Hartwigsen-Goedecker-Hutter, and generalized gradient approximation and the Perdew-Burke-Ernzerhof functional type including the norm-conserving ones on PSEUDODOJO [26], Hartwigsen-Goedecker-Hutter, and OPIUM-generated pseudopotentials. To ensure convergence, a plane-wave basis set with a cutoff energy of 45 hartrees was used. Both the cell parameters and internal coordinates were optimized with a force tolerance of  $5 \times 10^{-11}$  hartree/bohr. An unshifted *k*-point grid of  $18 \times 18 \times 18$  was employed in structural relaxation, which was found to yield converged results. To compensate the volume underestimation due to LDA, we applied a negative pressure of  $-5$  GPa during relaxation, which then yielded similar critical doping for the *T*-to-*C* transition compared with previous works [16–19]. The electron doping in BaTiO<sub>3</sub> is achieved by adding extra electrons to the system and compensating with uniform positive background charges. For the DFPT calculations of the electron-phonon coupling matrix, the Brillouin-zone integration was performed over an unshifted  $18 \times 18 \times 18$  grid with direction calculations on the same *k*-point grid and  $6 \times 6 \times 6$  *q*-point grid to obtain reasonably converged transport properties.

For comparison, the transport coefficients were calculated using two approaches, viz., the constant relaxation time approximation and variational approach, both being within the frame of Boltzmann's transport theory. The CRTA, as implemented in the BOLTZTRAP code [27,28], has been widely adopted in theoretical studies of thermoelectric properties, which only requires the computation of electronic band

structures. Here, an unshifted  $24 \times 24 \times 24$  *k*-point grid was employed in the direct DFT calculations, then further interpolated to a  $192 \times 192 \times 192$  *k*-grid in BOLTZTRAP. The electrical conductivity and Seebeck coefficient within CRTA can be expressed as

$$\sigma_{\alpha\beta} = \int \sigma_{\alpha\beta}(\epsilon) \left( -\frac{\partial f}{\partial \epsilon} \right) d\epsilon, \quad (1)$$

$$S_{\alpha\beta} = \frac{1}{eT} \frac{\int \sigma_{\alpha\beta}(\epsilon) (\epsilon - \epsilon_F) \left( -\frac{\partial f}{\partial \epsilon} \right) d\epsilon}{\int \sigma_{\alpha\beta}(\epsilon) \left( -\frac{\partial f}{\partial \epsilon} \right) d\epsilon}, \quad (2)$$

where  $e$  is the magnitude of the charge of an electron,  $T$  is temperature,  $\epsilon_F$  is the Fermi energy,  $f$  is the electron's probability distribution function, and  $\sigma_{\alpha\beta}(\epsilon)$  is the energy-dependent conductivity tensor defined as  $\sigma_{\alpha\beta}(\epsilon) = N_s e^2 \tau \sum_{\mathbf{k}} v_{\alpha}(\mathbf{k}) v_{\beta}(\mathbf{k}) \delta(\epsilon - \epsilon_{\mathbf{k}})$ , with  $N_s$  being a spin factor of 2 for the spin degenerate case,  $\tau$  being the constant relaxation time, and  $v_{\alpha}$  being the  $\alpha$  component of the electron velocity.

Alternatively, the Boltzmann transport equation can be solved by the variational method with the lowest-order variational approximation (LOVA) considering the main scattering mechanism due to electron-phonon coupling [29–31], as first derived by Allen [29]. The Eliashberg spectral function which measures the electron-phonon coupling (EPC) contribution of electrons at the Fermi level scattered by phonons with frequency  $\omega$  can be written as [30]

$$\alpha^2 F(\omega) = \frac{1}{2\pi N(\epsilon_F)} \sum_{\mathbf{q}\nu} \frac{\gamma_{\mathbf{q}\nu}}{\omega_{\mathbf{q}\nu}} \delta(\omega - \omega_{\mathbf{q}\nu}), \quad (3)$$

where the mode-resolved phonon linewidth  $\gamma_{\mathbf{q}\nu}$  according to the Fermi "golden rule" is

$$\gamma_{\mathbf{q}\nu} = 2\pi \omega_{\mathbf{q}\nu} \sum_{\mathbf{k}+\mathbf{q}j',\mathbf{k}j} |g_{\mathbf{k}+\mathbf{q}j',\mathbf{k}j}^{\mathbf{q}\nu}|^2 \delta(\epsilon_{\mathbf{k}j} - \epsilon_F) \delta(\epsilon_{\mathbf{k}+\mathbf{q}j'} - \epsilon_F), \quad (4)$$

with  $g_{\mathbf{k}+\mathbf{q},\mathbf{k}}^{\mathbf{q}\nu} = \tilde{\eta}_{\mathbf{q}\nu} / \sqrt{2M\omega_{\mathbf{q}\nu}} \langle \psi_{\mathbf{k}+\mathbf{q}} | \delta V^{\mathbf{q}\nu} | \psi_{\mathbf{k}} \rangle$  being the EPC matrix. And the EPC strength (or EPC constant)  $\lambda$  can be defined as

$$\begin{aligned} \lambda &= 2 \int_0^{\infty} d\omega \frac{\alpha^2 F(\omega)}{\omega} \\ &= \frac{\sum_{\mathbf{k}+\mathbf{q}j',\mathbf{k}j} \frac{|g_{\mathbf{k}+\mathbf{q}j',\mathbf{k}j}^{\mathbf{q}\nu}|^2}{\hbar\omega_{\mathbf{q}\nu}} \delta(\epsilon_{\mathbf{k}j} - \epsilon_F) \delta(\epsilon_{\mathbf{k}+\mathbf{q}j'} - \epsilon_F)}{\sum_{\mathbf{k}j} \delta(\epsilon_{\mathbf{k}j} - \epsilon_F)}, \end{aligned} \quad (5)$$

Note that in special cases with slightly soft phonon modes, a minimum frequency of  $10^{-6}$  hartrees is adopted to prevent divergent result.

For electrical resistivity, we adopt the elastic LOVA approach, where the Fermi-smearing effect is neglected. The associated EPC transport spectral function is defined as

$$\begin{aligned} \alpha_u^2 F_{\alpha\beta}(\omega) &= \frac{1}{N(\epsilon_F)} \sum_{\mathbf{q}\nu} \sum_{\mathbf{k}+\mathbf{q}j',\mathbf{k}j} \eta_{\mathbf{k}+\mathbf{q}j',\mathbf{k}j} |g_{\mathbf{k}+\mathbf{q}j',\mathbf{k}j}^{\mathbf{q}\nu}|^2 \\ &\quad \times \delta(\epsilon_{\mathbf{k}j} - \epsilon_F) \delta(\epsilon_{\mathbf{k}+\mathbf{q}j'} - \epsilon_F) \delta(\omega - \omega_{\mathbf{q}\nu}), \end{aligned} \quad (6)$$

with an efficiency factor [30]

$$\eta_{\mathbf{k}+\mathbf{q}j',\mathbf{k}j} = \frac{v_{\alpha}(\mathbf{k}j) \cdot v_{\beta}(\mathbf{k}j) - v_{\alpha}(\mathbf{k} + \mathbf{q}j') \cdot v_{\beta}(\mathbf{k}j)}{\langle v_{\alpha} \rangle \langle v_{\beta} \rangle}, \quad (7)$$

which quantifies the preferential weight of the backscattering process. Here,  $v_\alpha(\mathbf{k}j)$  is the  $\alpha$  component of electron velocity in state  $|\psi_{\mathbf{k}j}\rangle$ , with  $\langle v_\alpha \rangle$  being the average of the  $\alpha$

component of the Fermi velocity. The transport EPC constant can be defined as  $\lambda_{\text{tr}}(\alpha, \beta) = 2 \int_0^\infty d\omega \alpha_{\text{tr}}^2 F_{\alpha\beta}(\omega)/\omega$ , and the diagonal term in full reads

$$\lambda_{\text{tr}}(\alpha, \alpha) = \frac{\sum_{\mathbf{k}+\mathbf{q}j', \mathbf{k}j} \frac{(v_\alpha(\mathbf{k}+\mathbf{q}j') - v_\alpha(\mathbf{k}j))^2 |g_{\mathbf{k}+\mathbf{q}j', \mathbf{k}j}^{\mathbf{q}\nu}|^2}{\hbar\omega_{\mathbf{q}\nu}} \delta(\epsilon_{\mathbf{k}j} - \epsilon_{\text{F}}) \delta(\epsilon_{\mathbf{k}+\mathbf{q}j'} - \epsilon_{\text{F}})}{\sum_{\mathbf{k}j} v_\alpha(\mathbf{k}j)^2 \delta(\epsilon_{\mathbf{k}j} - \epsilon_{\text{F}})}. \quad (8)$$

In elastic LOVA, the electrical resistivity can be expressed in terms of  $\alpha_{\text{tr}}^2 F(\omega)$  as follows:

$$\rho_{\alpha\beta}(T) = \frac{\pi V_{\text{cell}} k_B T}{N(\epsilon_{\text{F}})} \int_0^\infty \frac{d\omega}{\omega} \frac{x^2}{\sinh^2 x} \alpha_{\text{tr}}^2 F_{\alpha\beta}(\omega), \quad (9)$$

where  $x$  is  $\hbar\omega/(2k_B T)$ , and  $V_{\text{cell}}$  is the volume of the unit cell.

To calculate the Seebeck coefficient, Fermi smearing has to be considered explicitly; hence, we adopt the inelastic LOVA [31]:

$$S = -\frac{\pi k_B}{\sqrt{3}e} \frac{(Q_{01}^{-1})_{\alpha\beta}}{(Q_{00}^{-1})_{\alpha\beta}} \approx \frac{\pi k_B}{\sqrt{3}e} \sum_{\gamma} (Q_{01})_{\alpha\gamma} (Q_{11}^{-1})_{\gamma\beta}, \quad (10)$$

where  $(Q_{nm'})_{\alpha\beta}$  is the scattering operator involving electron-phonon scattering with absorption and emission of phonons:

$$(Q_{nm'})_{\alpha\beta} = \frac{2\pi V_{\text{cell}} N(\epsilon_{\text{F}})}{\hbar k_B T} \int d\epsilon d\epsilon' d\omega \sum_{s, s'=\pm 1} f(\epsilon)[1-f(\epsilon')]\{[n(\omega)+1]\delta(\epsilon-\epsilon'-\hbar\omega) + n(\omega)\delta(\epsilon-\epsilon'+\hbar\omega)\} \\ \times \alpha_{\text{Allen}}^2 F(s, s', \alpha, \beta, \epsilon, \epsilon', \omega) \times J(s, s', n, n', \epsilon, \epsilon'), \quad (11)$$

where  $\hbar$  is the reduced Planck constant,  $n$  is the Bose-Einstein distribution,  $\omega$  is the phonon frequency, and  $J$  is the joint energy polynomial. The transport spectral function here is defined as

$$\alpha_{\text{Allen}}^2 F(s, s', \alpha, \beta, \epsilon, \epsilon', \omega) = \frac{1}{2N(\epsilon_{\text{F}})} \sum_{\mathbf{k}, \mathbf{k}+\mathbf{q}} |g_{\mathbf{k}+\mathbf{q}, \mathbf{k}}^{\mathbf{q}\nu}|^2 \delta(\epsilon_{\mathbf{k}} - \epsilon) \delta(\epsilon_{\mathbf{k}+\mathbf{q}} - \epsilon') \delta(\omega - \omega_{\mathbf{q}}) \\ \times [F_\alpha(\mathbf{k}) - sF_\alpha(\mathbf{k}')][F_\beta(\mathbf{k}) - s'F_\beta(\mathbf{k}')]. \quad (12)$$

More details about the VA method of a nonmagnetic metal can be found in Refs. [29,31].

### III. RESULTS AND DISCUSSION

#### A. Doping-induced tetragonal-to-cubic transition

First, let us examine the structural evolution in the  $T$  phase of BaTiO<sub>3</sub> upon electron doping. Without introduction of electrons, we obtain an in-plane lattice constant  $a$  of 3.962 Å and  $c/a$  ratio of 1.018 for the  $T$  phase. These values are in good agreement with experimental measurements, i.e., 3.986 Å and 1.010, respectively [32]. As illustrated in Fig. 1(a), in the  $T$  phase, the Ti<sup>4+</sup> ion shifts upwards from its high-symmetry position, while the elongated oxygen octahedron moves downwards relative to the Ba<sup>2+</sup> ions. The calculated Ti offset from the equatorial O<sub>I</sub> plane  $z_{\text{Ti}} - z_{\text{O}_I}$  is 0.120 Å, which is consistent with previous reports [16–19].

With electron doping, BaTiO<sub>3</sub> becomes metallic and the polarization is ill-defined since long-range Coulomb interactions are screened by itinerant electrons [33,34]. Hence, we analyze the changes in structural parameters, i.e., atomic displacements and the  $c/a$  ratio, to characterize the phase transition. As the electron concentration increases, the tetragonality, characterized by the  $c/a$  ratio and fractional atomic displacements, initially remains stable (Fig. 1) until a

concentration of  $\sim 0.06$  e/f.u. (or  $9.36 \times 10^{20} \text{cm}^{-3}$ ), which we can refer to as the first critical doping concentration  $n_{c1}$ . Nevertheless, the additional electrons within this doping range introduce a volumetric effect, which increases linearly. Upon further increment of doping, the  $c/a$  ratio gradually decreases to unity at a critical doping concentration of  $n_{c2} = 0.115$  e/f.u. (or  $1.79 \times 10^{21} \text{cm}^{-3}$ ), and the polar displacements reduce concomitantly to zero, i.e., all atoms adopt their high-symmetry positions, indicating that the structure transforms into the cubic phase. Interestingly, the volume change upon doping is nonmonotonic, showing a slight shrinkage following the initial linear increase and a rapid growth within the cubic phase, which is due to the linearly increasing  $a$  and the variation of  $c/a$ . These doping-induced structural changes agree with previous calculations [16–19]. Moreover, the critical doping concentration for the transition from tetragonal-to-cubic phase closely matches the experimental value of  $1.9 \times 10^{21} \text{cm}^{-3}$  in oxygen-deficient BaTiO<sub>3- $\delta$</sub>  [20,23].

#### B. Transport properties vs doping with CRTA

The doping-induced structural variation—albeit continuous and seemingly rather minute—can lead to significant changes in the electronic band structure, phonon dispersion, EPC, and consequently the transport properties. In the

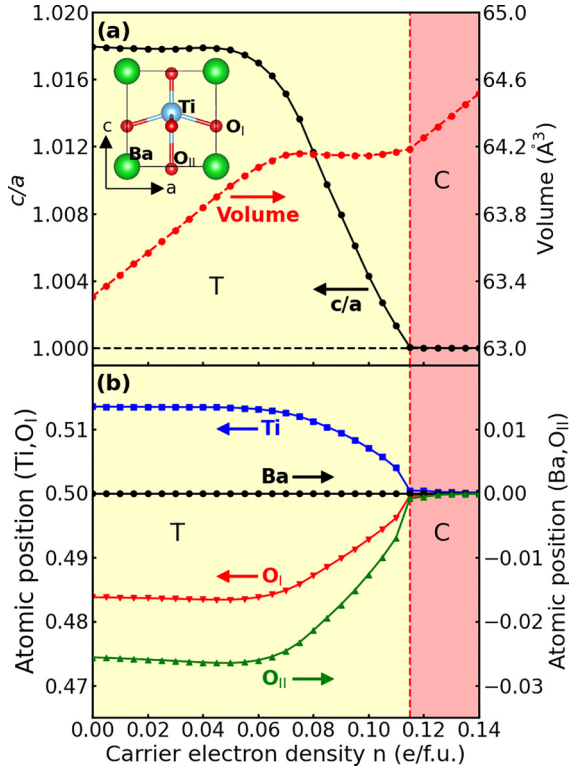


FIG. 1. DFT-predicted structural evolution of BaTiO<sub>3</sub> as a function of electron-doping concentration. (a) Tetragonality ( $c/a$  ratio) and volume of the unit cell. The inset shows the unit-cell structure of the  $T$  phase. (b) Atomic positions taking Ba as reference.

following, we begin with the CRTA approach, where the relaxation time is treated as a constant and the transport properties depend solely on the electron band structure. Note that only  $\sigma_{\alpha\beta}/\tau$  (or  $\rho_{\alpha\beta}\tau$ ) can be computed by CRTA, rather than the conductivity (or resistivity). To assess the doping effect on the transport properties, let us consider a representative temperature of 300 K; the CRTA results are shown in Fig. 2. As expected, the resistivity decreases with electron doping, and in particular, the in-plane component  $\rho_{xx}\tau$  decreases monotonically with a decreasing slope, while the out-of-plane component  $\rho_{zz}\tau$  is large at low doping but shows a fast decrease for doping above  $n_{c1} = 0.06$  e/f.u. Subsequently, the in-plane and out-of-plane components become identical beyond  $n_{c2} = 0.115$  e/f.u., indicating a transition to the cubic phase.

The CRTA-calculated Seebeck coefficient is depicted in Fig. 2(b), which displays more intricate features than conductivity. The Seebeck values are negative since electrons are the charge carriers. With increasing doping, the magnitude of  $S_{xx}$  first declines, reaches a minimum at  $n_{c1}$ , then rises slightly, and decreases again within the cubic phase. On the other hand,  $|S_{zz}|$  exhibits more significant nonmonotonic variations, first decreasing with an upturning point at 0.02 e/f.u., followed by a rapid increase with a downturning point at  $n_{c1}$ , after which a continuous decrease follows. It is interesting to note that the largest difference between the in-plane and out-of-plane components occurs at  $n_{c1}$ , and it gradually diminishes with further doping until the anisotropy disappears at  $n_{c2} = 0.115$  e/f.u., where the  $T$ -to- $C$  transition occurs. The overall Seebeck

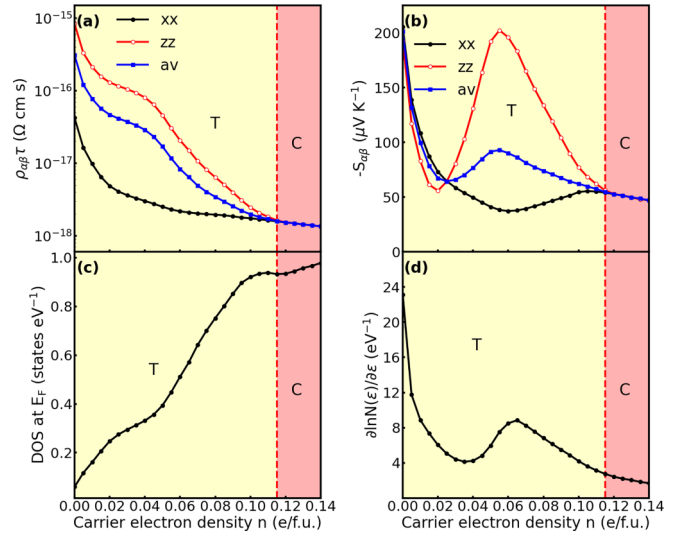


FIG. 2. CRTA-calculated transport properties of BaTiO<sub>3</sub> as a function of electron-doping concentration at room temperature (300 K). The in-plane, out-of-plane, and diagonal-average of (a) the electrical conductivity divided by a constant relaxation time, and (b) the Seebeck coefficient; (c) Electronic density of states (DOS)  $N$  and (d) derivative of  $\ln N(\epsilon)$  with respect to energy at the Fermi level.

coefficient  $S_{av}$  (blue solid line) obtained by averaging the trace of  $S_{\alpha\beta}$  is also plotted, showing a qualitatively similar trend to that of  $S_{zz}$ . The experimental data for the tetragonal phase of doped BaTiO<sub>3</sub> at 300 K are  $-401$   $\mu\text{V/K}$  [23] with an electron concentration of  $2.0 \times 10^{20}$   $\text{cm}^{-3}$ , which is significantly larger than our CRTA value of  $-93$   $\mu\text{V/K}$  at the same concentration. On the other hand, our predicted magnitudes are similar to previous CRTA calculated values [18], and the discrepancy (within 20%) is likely due to the difference in computational details, such as the pseudopotential types and in consequence the lattice constants.

The abovementioned doping dependence of the Seebeck coefficient can be easily understood by the Mott relation [18,35,36]:

$$S = -\frac{\pi^2 k_B^2 T}{3e} \left[ \frac{d \ln \sigma(\epsilon)}{d\epsilon} \right]_{\epsilon=\epsilon_F} = -\frac{\pi^2 k_B^2 T}{3e} \left[ \frac{\partial \ln N(\epsilon)}{\partial \epsilon} + \frac{\partial \ln v^2(\epsilon)}{\partial \epsilon} + \frac{\partial \ln \tau(\epsilon)}{\partial \epsilon} \right]_{\epsilon=\epsilon_F}, \quad (13)$$

where  $v(\epsilon)$  is the average electron velocity at a certain energy. Assuming a relatively weak energy dependence of the velocity  $v(\epsilon)$  and relaxation time  $\tau(\epsilon)$ , the variation of  $S$  is dominated by the energy derivative of density of states (DOS), i.e.,  $1/N(\epsilon)(\partial N(\epsilon)/\partial \epsilon)$ . Both the DOS at the Fermi level and  $1/N(\epsilon)(\partial N(\epsilon)/\partial \epsilon)$  as a function of doping concentration are shown in Figs. 2(c) and 2(d), respectively. Although electron doping yields a monotonically increasing DOS, the energy derivative is nonmonotonic and the doping dependency well resembles that of the average Seebeck coefficient [blue line in Fig. 2(b)].

To understand the nature of the turning points in the Seebeck coefficient, we plot the band structure and the corresponding Fermi surface in Fig. 3. In the  $T$  phase, the three

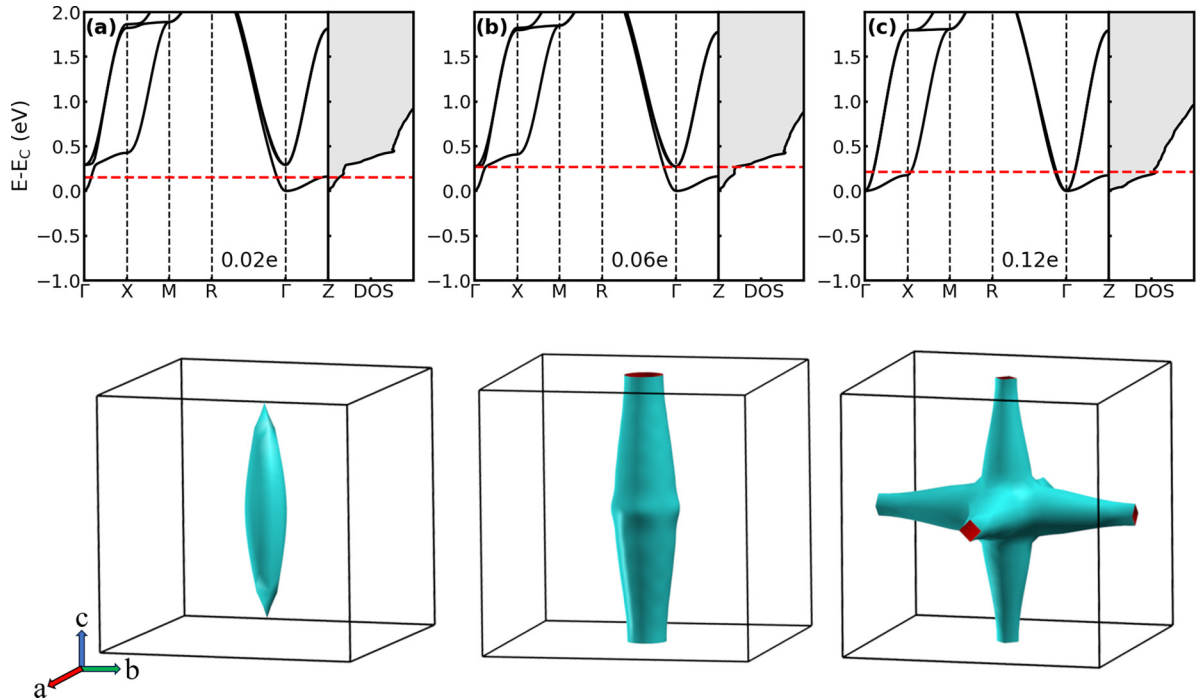


FIG. 3. Calculated electronic band structure and the corresponding Fermi surface of BaTiO<sub>3</sub> at electron-doping concentrations of (a) 0.02 e/f.u., (b) 0.06 e/f.u., and (c) 0.12 e/f.u. Zero energy is set at the bottom of the conduction band. The red dashed line denotes the Fermi energy.

$t_{2g}$  bands of Ti split into a low-lying single  $d_{xy}$  band and two high-lying  $d_{xz}$  and  $d_{yz}$  bands being degenerate at the  $\Gamma$  point. We numerically find that interestingly, adding electrons below the level of  $n_{c1}$  mainly causes the Fermi level to rise with negligible effect on the band structure, while above  $n_{c1}$  the tetragonality starts to decrease and the splitting of the  $t_{2g}$  bands shrinks until they coalesce at  $n_{c2}$ . This is consistent with the structural change shown in Fig. 1(a). At the doping concentration of 0.02 e/f.u., although no obvious structural change occurs, it is a special doping that the Fermi surface nearly reaches the Brillouin-zone boundary Z point, and the corresponding DOS has a kink dividing two different slopes. It is the asymmetry of DOS across the Fermi energy at this critical doping which yields the upturn of the Seebeck coefficient. At  $n_{c1}$  of 0.06 e/f.u., the Fermi surface grows larger and forms tubes along the  $z$  direction, and more importantly, it is a critical level that the Fermi level reaches the bottom of the high-lying  $t_{2g}$  bands. Another kink can be seen in the DOS at this doping, above which the DOS shows a rapid increase and such asymmetry causes  $S$  to decrease. With more electrons above  $n_{c1}$ , two spherically shaped inner Fermi surfaces (not visible in Fig. 3) emerge and the outer Fermi surface changes into a “star” shape that becomes isotropic at  $n_{c2}$ .

For comparison, we also examine scenarios without structural relaxation, in which the structure of  $T$ -phase BaTiO<sub>3</sub> remains fixed. This approach is commonly adopted in computational studies of thermoelectric properties where the band structure is frozen and the only doping effect is the shift of the Fermi level. Both the  $\sigma_{\alpha\beta}/\tau$  and  $S_{\alpha\beta}$  exhibit similar behaviors to those of the relaxed structures, whereas the main difference is the persistent anisotropy due to the absence of  $T$ -to- $C$  transition. The details are shown in Fig. S1 of the Supplemental Material [37].

When the doping concentration approaches the critical doping of  $n_{c2}$ , the DOS is close to another kink [Fig. 3(c) and Fig. S2], which indeed cause a change of slope in both the conductivity and Seebeck coefficient (Fig. 2). However, near the  $T$ -to- $C$  transition point, both the CRTA conductivity and Seebeck coefficient vary smoothly with respect to the change of doping without showing critical behaviors. This is in contrast to the expectation from the strong electron-phonon coupling in this region [19], which is not considered explicitly in the CRTA approach.

### C. Transport properties vs doping with explicit electron-phonon coupling

In the following, we take the fully *ab initio* EPC into account via the VA method. The calculated phonon-dispersion curves with linewidths at four representative doping concentrations are shown in Fig. 4. In agreement with Ref. [19], while most of the phonon branches show relatively small changes upon doping, we also find three softening polar optical phonon modes (blue markers in Fig. 4, two being degenerate in the  $T$  phase and three being degenerate in the  $C$  phase) at the  $\Gamma$  point with their minima around the  $T$ -to- $C$  transition point, suggesting that the phase transition is driven by the instability of these softening modes. It should be noted that small imaginary frequencies near the  $\Gamma$  point tend to occur for doping concentration close to the  $T$ -to- $C$  transition. We numerically find that this minor soft phonon is computationally difficult to avoid, which is believed to be related to the instability in maintaining the tetragonal structure. The phonon linewidths indicate that strong electron-phonon coupling is concentrated around the softening modes of the  $\Gamma$  point and a high-lying optical branch between  $\Gamma$  and Z points. The most significant change in EPC occurs only to the  $\Gamma$ -point

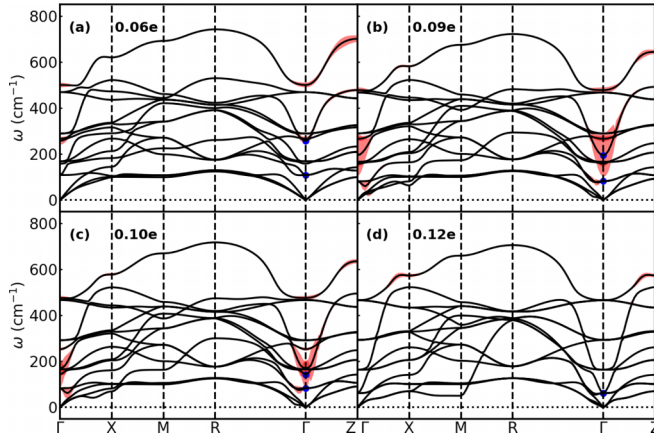


FIG. 4. Calculated phonon-dispersion curves and phonon linewidths of BaTiO<sub>3</sub> at doping concentrations of (a) 0.06 e/f.u., (b) 0.09 e/f.u., (c) 0.10 e/f.u., and (d) 0.12 e/f.u. The red broadening shows the phonon linewidths and the blue dots denote the softening optical modes at  $\Gamma$  point.

softening modes, which are much strengthened near the  $T$ -to- $C$  transition. For doping levels away from the transition point, e.g., below 0.06 e/f.u. of the  $T$  phase or beyond 0.12 e/f.u. of the  $C$  phase, the phonon linewidth decreases to a much lower level. The enhancement of phonon linewidths of the  $\Gamma$ -point softening modes above 0.06 e/f.u. doping is correlated to the increase of the Fermi nesting factor at the  $\Gamma$  point, as shown in Fig. S3 of the Supplemental Material [37].

The synergy of low phonon frequencies and strong EPC (large linewidths) of the softening modes gives rise to a much enhanced EPC constant, since the mode-resolved EPC constant  $\lambda_{qv}$  is proportional to  $\gamma_{qv}/\omega_{qv}^2$ , which is strongly influenced by the softening polar phonons and the enhanced Fermi nesting [38]. The calculated total EPC constant  $\lambda$  is plotted in Fig. 5(a) (black line) for doping concentrations between 0.06 and 0.14 e/f.u., and note that the VA method is

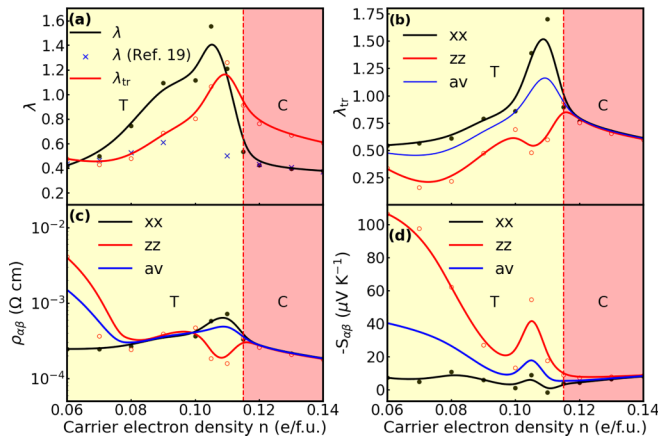


FIG. 5. VA-calculated transport-related properties of BaTiO<sub>3</sub> as a function of doping concentration. (a) EPC strength  $\lambda$  (black solid line) and the overall transport EPC strength  $\lambda_{tr}$  (red solid line). (b) The in-plane, out-of-plane, and diagonal-average of the transport EPC strength  $\lambda_{tr}$ , (c) the electrical resistivity, and (d) the Seebeck coefficient.

not applicable to systems with insufficient amount of charge carriers; in other words, it may fail to yield quantitative results for low doping cases if the Fermi level is close to the conduction-band edge. The calculated  $\lambda$  exhibits a strong increase with doping and peaks in the vicinity of the critical concentration  $n_{c2}$  in the  $T$  phase, then falls dramatically after transforming into the cubic phase. Below 0.07 e/f.u. in the tetragonal phase or above 0.11 e/f.u. in the cubic phase, the magnitudes of our predicted  $\lambda$  are very close to the values reported in Ref. [19]. In the vicinity of the transition point, our prediction appears larger, but the general trend is consistent between both works. The discrepancy is related to the fact that the softening phonons at the  $\Gamma$  point have a strong influence on the EPC constant [see Eq. (5)], given that these frequencies are rather sensitive to the computational details.

In Figs. 5(a) and 5(b), we also plot the overall transport EPC constant  $\lambda_{tr} = 2 \int_0^\infty d\omega \alpha^2 F_{tr}(\omega)/\omega$  and its in-plane and out-of-plane components, respectively. In the  $T$  phase, the in-plane transport EPC constant is numerically found to be larger than the out-of-plane component. And, it is interesting to note that  $\lambda_{tr}$  is consistently lower than  $\lambda$  in the  $T$  phase, while in the  $C$  phase  $\lambda_{tr}$  is larger than  $\lambda$ . The key distinction between  $\lambda$  and  $\lambda_{tr}$  lies in the weight of spectral function  $\alpha_{tr}^2 F(\omega)$  by the Fermi velocities compared to  $\alpha^2 F(\omega)$  in Eq. (5) and Eq. (8), respectively (see Fig. S4 in the Supplemental Material [37]). A likely explanation for the reduced  $\lambda_{tr}$  is that the strongly nested EPC associated with the  $\Gamma$ -point softening phonons is partially suppressed by the  $z$  component of the  $(v_{kj} - v_{k+qj})^2$  term in  $\alpha_{tr}^2 F(\omega)$  (see Eq. (8) and Ref. [38]), since the Fermi surface has the square-like shape and the Fermi velocities in the  $d_{xy}$  band connected by small  $\mathbf{q}$  vectors are nearly equal.

The VA-calculated electrical resistivity  $\rho$  contributed by EPC is shown in Fig. 5(c), which exhibits a qualitatively similar doping dependence as  $\lambda_{tr}$ . Below 0.08 e/f.u., the general trend is consistent with the CRTA results [Fig. 2(a)] that the out-of-plane component of resistivity is larger than the in-plane component, but a remarkable distinction can be seen when the doping concentration approaches the transition point: The overall  $\rho$  shows an obvious peak around 0.11 e/f.u. with VA, which is missing in the  $\rho$  computed by the CRTA method. In particular, the in-plane component  $\rho_{xx}$  shows a significant enhancement between 0.10 and 0.12 e/f.u., whereas the out-of-plane component  $\rho_{zz}$  has a critical decrease in this doping range. For doping levels beyond 0.12 e/f.u., BaTiO<sub>3</sub> transforms into the cubic structure and the resistivity tensor becomes isotropic with reduced values. According to Eq. (9) and the fact that both  $N(\epsilon_F)$  and  $\langle v_\alpha \rangle$  change smoothly across the  $T$ -to- $C$  phase transition, the substantial increases in electrical resistivity in both directions are evidently due to the corresponding increase in the transport EPC constant  $\lambda_{tr}$ , as illustrated in Fig. 5(b). The average resistivity  $\rho_{av}$  of  $2.86 \times 10^{-4}$  and  $1.83 \times 10^{-4}$   $\Omega$  cm with the electron concentration of 0.07 and 0.14 e/f.u. ( $1.1 \times 10^{21}$  and  $2.2 \times 10^{21}$   $\text{cm}^{-3}$ ), respectively, agree reasonably with the experimental value of  $2.99 \times 10^{-4}$   $\Omega$  cm in BaTiO<sub>3- $\delta$</sub>  [20,23] extrapolated to the same concentration and  $2.33 \times 10^{-4}$   $\Omega$  cm with electron concentration of  $4.6 \times 10^{21}$   $\text{cm}^{-3}$  in BaNb<sub>0.5</sub>Ti<sub>0.5</sub>O<sub>3</sub> thin film [39]. The discrepancy can be partly ascribed to the residual resistivity from impurity scatterings which is neglected in the calculations.

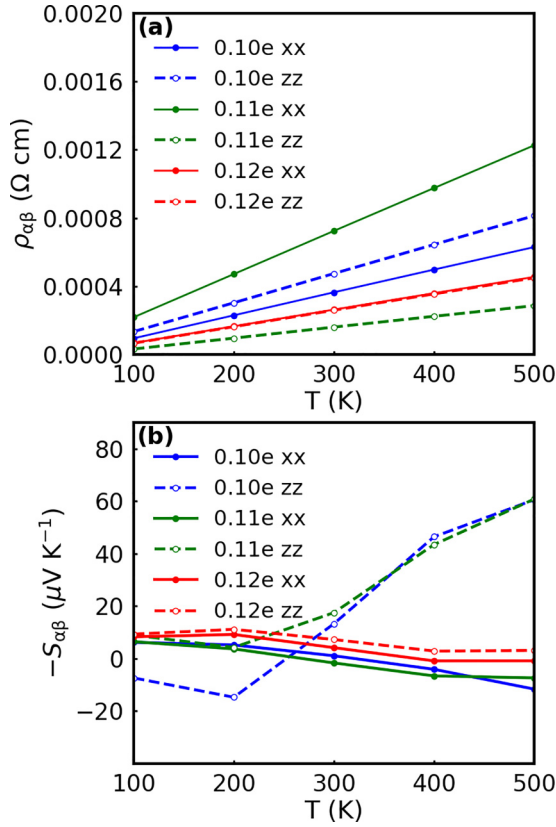


FIG. 6. VA-calculated transport properties as a function of temperature of BaTiO<sub>3</sub> for selected doping concentrations near the *T*-to-*C* transition, i.e., 0.10 e/f.u., 0.11 e/f.u., and 0.12 e/f.u. The in-plane and out-of-plane components of (a) the electrical resistivity and (b) the Seebeck coefficient.

Figure 5(d) illustrates the VA-calculated Seebeck coefficient of BaTiO<sub>3</sub> upon doping. Comparing the  $S$  computed from CRTA and VA, below 0.10 e/f.u. the general trends of decreasing magnitude with doping and  $S_{zz}$  being much larger than  $S_{xx}$  are in good agreement, but between 0.10 and 0.12 e/f.u., i.e., near the critical concentration of the phase transition, both components of VA-calculated  $S$  show substantial changes that were not observed in the CRTA result [see Fig. 2(b)]. Therefore, explicit consideration of electron-phonon coupling in VA can yield critical enhancements of both the resistivity and Seebeck coefficient near the *T*-to-*C* transition point, whereas the CRTA method, which neglects specific scattering mechanisms, especially the electron-phonon scattering with strong doping dependence of the phonon dispersion and EPC, fails qualitatively to predict the transport properties in this regime.

#### D. Temperature effect on the transport properties

Finally, we further explore the temperature effect on the transport coefficients near the transition point, i.e., between 0.10 and 0.12 e/f.u., which are shown in Fig. 6. However, note that any possible phase transition(s) purely induced by temperature is not considered here. For all the selected doping concentrations, both  $\rho_{xx}$  and  $\rho_{zz}$  increase linearly with temperature [see Fig. 6(a)], which is a typical behavior for metals

at elevated temperatures. And interestingly, the temperature dependence of resistivity is found to be proportional to its magnitude, i.e., larger  $\rho_{\alpha\beta}$  shows a larger slope with respect to temperature.

The temperature dependence of the Seebeck coefficient is monotonic in the cubic phase [see the red curves in Fig. 6(b)], whose magnitude decreases with increasing temperature. In the tetragonal phase, however,  $S$  exhibits a more complex behavior.  $S_{xx}$  decreases monotonously but shows a reversed sign (negative to positive) at about 320 K, indicating that the charge carriers dominating the thermoelectric effect change from electrons to holes in the in-plane direction. In the *z* direction,  $S_{zz}$  generally increases with temperature, with a few positive values at low temperature for the doping of 0.10 e/f.u. Nevertheless, we demonstrate that the critical enhancement of the transport properties can be more prominent by increasing the temperature.

However, it is worth noting that temperature can have manifold influences in reality, for instance the phase transitions, the finite-temperature phonons, the thermal expansion, etc. It was known that the doping concentration of the *T*-to-*C* transition decreases at increased temperature [20,22], so that the critical behavior can be achieved at a lower dopant level; e.g., it was reported that the *T*-to-*C* transition occurs with only about  $3.6 \times 10^{20} \text{cm}^{-3}$  at 300 K [20,40]. Moreover, strain engineering in BaTiO<sub>3</sub> thin films is also an effective tool to further tune the transition point and hence the transport properties [41,42].

#### IV. SUMMARY

In summary, we have studied the effect of electron doping on the electronic transport properties of BaTiO<sub>3</sub> using density-functional theory and density-functional perturbation theory within the frame of Boltzmann's transport theory. The electrical resistivity and Seebeck coefficient are computed with two methods, viz., the constant relaxation time approximation and the variational approach considering electron-phonon coupling. For low-doping concentrations, where the structure remains tetragonal, the smooth variations of the transport coefficients can be well explained by the evolution of the electronic band structure. But, in the vicinity of doping-induced tetragonal-to-cubic phase transition, anomalies in the resistivity and Seebeck coefficient are found only with the more accurate variational approach with explicit consideration of electron-phonon scatterings, which are due to coupling of itinerant electrons with soft polar phonon modes. We hope our predictions will be experimentally checked soon, and it is desirable to understand the correlation between the nature of the phase transition and the transport properties along the phase boundary of the temperature-doping phase diagram of BaTiO<sub>3</sub>.

#### ACKNOWLEDGMENTS

This work is supported by the National Natural Science Foundation of China under Grant No. 12074277, Projects of International Cooperation and Exchanges NSFC (Grant No. 12311530693), the startup fund from Soochow University and the support from Priority Academic Program Development (PAPD) of Jiangsu Higher Education Institutions.

- [1] P. W. Anderson and E. I. Blount, Symmetry considerations on martensitic transformations: “Ferroelectric” metals? *Phys. Rev. Lett.* **14**, 217 (1965).
- [2] S. Lee, J. A. Bock, S. Trolier-McKinstry, and C. A. Randall, Ferroelectric-thermoelectricity and Mott transition of ferroelectric oxides with high electronic conductivity, *J. Eur. Ceram. Soc.* **32**, 3971 (2012).
- [3] H. Sakai, K. Ikeura, M. S. Bahramy, N. Ogawa, D. Hashizume, J. Fujioka, Y. Tokura, and S. Ishiwata, Critical enhancement of thermopower in a chemically tuned polar semimetal  $\text{MoTe}_2$ , *Sci. Adv.* **2**, e1601378 (2016).
- [4] M. J. Laubitz and T. Matsumura, Transport properties of the ferromagnetic metals. I. Cobalt, *Can. J. Phys.* **51**, 1247 (1973).
- [5] S. J. Watzman, R. A. Duine, Y. Tserkovnyak, S. R. Boona, H. Jin, A. Prakash, Y. Zheng, and J. P. Heremans, Magnon-drag thermopower and Nernst coefficient in Fe, Co, and Ni, *Phys. Rev. B* **94**, 144407 (2016).
- [6] N. Ni, S. Nandi, A. Kreyssig, A. I. Goldman, E. D. Mun, S. L. Bud’ko, and P. C. Canfield, First-order structural phase transition in  $\text{CaFe}_2\text{As}_2$ , *Phys. Rev. B* **78**, 014523 (2008).
- [7] S. Röbber, D. Cherian, M. Doerr, C. Koz, C. Curfs, Y. Prots, U. K. Röbber, U. Schwarz, S. Elizabeth, and S. Wirth, First-order structural transition in the magnetically ordered phase of  $\text{Fe}_{1.13}\text{Te}$ , *Phys. Rev. B* **84**, 174506 (2011).
- [8] D. Byeon, R. Sobota, K. Delime-Codrin, S. Choi, K. Hirata, M. Adachi, M. Kiyama, T. Matsuura, Y. Yamamoto, M. Matsunami, and T. Takeuchi, Discovery of colossal Seebeck effect in metallic  $\text{Cu}_2\text{Se}$ , *Nat. Commun.* **10**, 72 (2019).
- [9] R. Hauser, E. Bauer, and E. Gratz, Pressure-dependent electrical resistivity of  $R\text{Co}_2$  compounds ( $R$  = rare earth), *Phys. Rev. B* **57**, 2904 (1998).
- [10] C. N. Kuo, H. F. Liu, C. S. Lue, L. M. Wang, C. C. Chen, and Y. K. Kuo, Characteristics of the phase transition near 147 K in  $\text{Sr}_3\text{Ir}_4\text{Sn}_{13}$ , *Phys. Rev. B* **89**, 094520 (2014).
- [11] C. N. Kuo, C. W. Tsen, C. M. Wang, C. Y. wang, Y. R. Chen, L. M. Wang, C. F. Lin, K. K. Wu, Y. K. Kuo, and C. S. Lue, Lattice distortion associated with Fermi-surface reconstruction in  $\text{Sr}_3\text{Rh}_4\text{Sn}_{13}$ , *Phys. Rev. B* **91**, 165141 (2015).
- [12] C. N. Kuo, W. T. Chen, C. W. Tseng, C. J. Hsu, R. Y. Huang, F. C. Chou, Y. K. Kuo, and C. S. Lue, Evidence for a second-order phase transition around 350 K in  $\text{Ce}_3\text{Rh}_4\text{Sn}_{13}$ , *Phys. Rev. B* **97**, 094101 (2018).
- [13] S. Katayama and D. L. Mills, Theory of anomalous resistivity associated with structural phase transitions in IV-VI compounds, *Phys. Rev. B* **22**, 336 (1980).
- [14] R.-z. Zhang, X.-y. Hu, P. Guo, and C.-l. Wang, Thermoelectric transport coefficients of n-doped  $\text{CaTiO}_3$ ,  $\text{SrTiO}_3$  and  $\text{BaTiO}_3$ : A theoretical study, *Phys. B: Condens. Matter* **407**, 1114 (2012).
- [15] C. J. Johnson, Some dielectric and electro-optic properties of  $\text{BaTiO}_3$  single crystals, *Appl. Phys. Lett.* **7**, 221 (1965).
- [16] Y. Iwazaki, T. Suzuki, Y. Mizuno, and S. Tsuneyuki, Doping-induced phase transitions in ferroelectric  $\text{BaTiO}_3$  from first-principles calculations, *Phys. Rev. B* **86**, 214103 (2012).
- [17] X. He and K.-j. Jin, Persistence of polar distortion with electron doping in lone-pair driven ferroelectrics, *Phys. Rev. B* **94**, 224107 (2016).
- [18] H. Saijo, K. Yamauchi, K. Shirai, and T. Oguchi, Impact of ferroelectric distortion on thermopower in  $\text{BaTiO}_3$ , *J. Phys. Soc. Jpn.* **84**, 054701 (2015).
- [19] J. Ma, R. Yang, and H. Chen, A large modulation of electron-phonon coupling and an emergent superconducting dome in doped strong ferroelectrics, *Nat. Commun.* **12**, 2314 (2021).
- [20] T. Kolodiazhnyi, M. Tachibana, H. Kawaji, J. Hwang, and E. Takayama-Muromachi, Persistence of ferroelectricity in  $\text{BaTiO}_3$  through the insulator-metal transition, *Phys. Rev. Lett.* **104**, 147602 (2010).
- [21] I. K. Jeong, S. Lee, S.-Y. Jeong, C. J. Won, N. Hur, and A. Llobet, Structural evolution across the insulator-metal transition in oxygen-deficient  $\text{BaTiO}_{3-\delta}$  studied using neutron total scattering and Rietveld analysis, *Phys. Rev. B* **84**, 064125 (2011).
- [22] S. Bhowal and N. A. Spaldin, Polar metals: Principles and prospects, *Annu. Rev. Mater. Res.* **53**, 53 (2023).
- [23] J. Hwang, T. Kolodiazhnyi, J. Yang, and M. Couillard, Doping and temperature-dependent optical properties of oxygen-reduced  $\text{BaTiO}_{3-\delta}$ , *Phys. Rev. B* **82**, 214109 (2010).
- [24] X. Gonze, B. Amadon, G. Antonius, F. Arnardi, L. Baguet, J.-M. Beuken, J. Bieder, F. Bottin, J. Bouchet, E. Bousquet, N. Brouwer, F. Bruneval, G. Brunin, T. Cavignac, J.-B. Charraud, W. Chen, M. Côté, S. Cottenier, J. Denier, G. Geneste, P. Ghosez, M. Giantomassi, Y. Gillet, O. Gingras, D. R. Hamann, G. Hautier, X. He, N. Helbig, N. Holzwarth, Y. Jia, F. Jollet, W. Lafargue-Dit-Hauret, K. Lejaeghere, M. A. L. Marques, A. Martin, C. Martins, H. P. C. Miranda, F. Naccarato, K. Persson, G. Petretto, V. Planes, Y. Pouillon, S. Prokhorenko, F. Ricci, G.-M. Rignanese, A. H. Romero, M. M. Schmitt, M. Torrent, M. J. van Setten, B. V. Troeye, M. J. Verstraete, G. Zérah, and J. W. Zwanziger, The Abinit project: Impact, environment and recent developments, *Comput. Phys. Commun.* **248**, 107042 (2020).
- [25] A. H. Romero, D. C. Allan, B. Amadon, G. Antonius, T. Applencourt, L. Baguet, J. Bieder, F. Bottin, J. Bouchet, E. Bousquet, F. Bruneval, G. Brunin, D. Caliste, M. Côté, J. Denier, C. Dreyer, P. Ghosez, M. Giantomassi, Y. Gillet, O. Gingras, D. R. Hamann, G. Hautier, F. Jollet, G. Jomard, A. Martin, H. P. C. Miranda, F. Naccarato, G. Petretto, N. A. Pike, V. Planes, S. Prokhorenko, T. Rangel, F. Ricci, G.-M. Rignanese, M. Royo, M. Stengel, M. Torrent, M. J. van Setten, B. V. Troeye, M. J. Verstraete, J. Wiktor, J. W. Zwanziger, and X. Gonze, ABINIT: Overview and focus on selected capabilities, *J. Chem. Phys.* **152**, 124102 (2020).
- [26] M. J. van Setten, M. Giantomassi, E. Bousquet, M. J. Verstraete, D. R. Hamann, X. Gonze, and G. M. Rignanese, The PseudoDojo: Training and grading a 85 element optimized norm-conserving pseudopotential table, *Comput. Phys. Commun.* **226**, 39 (2018).
- [27] G. K. H. Madsen and D. J. Singh, BoltzTraP. A code for calculating band-structure dependent quantities, *Comput. Phys. Commun.* **175**, 67 (2006).
- [28] G. K. H. Madsen, J. Carrete, and M. J. Verstraete, BoltzTraP2, a program for interpolating band structures and calculating semiclassical transport coefficients, *Comput. Phys. Commun.* **231**, 140 (2018).
- [29] P. B. Allen, New method for solving Boltzmann’s equation for electrons in metals, *Phys. Rev. B* **17**, 3725 (1978).
- [30] S. Y. Savrasov and D. Y. Savrasov, Electron-phonon interactions and related physical properties of metals from linear-response theory, *Phys. Rev. B* **54**, 16487 (1996).
- [31] B. Xu, M. D. Gennaro, and M. J. Verstraete, Thermoelectric properties of elemental metals from first-principles electron-phonon coupling, *Phys. Rev. B* **102**, 155128 (2020).

- [32] G. Shirane, H. Danner, and R. Pepinsky, Neutron diffraction study of orthorhombic BaTiO<sub>3</sub>, *Phys. Rev.* **105**, 856 (1957).
- [33] R. E. Cohen, Origin of ferroelectricity in perovskite oxides, *Nature (London)* **358**, 136 (1992).
- [34] R. E. Cohen, Theory of ferroelectrics: A vision for the next decade and beyond, *J. Phys. Chem. Solids* **61**, 139 (2000).
- [35] M. Cutler and N. F. Mott, Observation of Anderson localization in an electron gas, *Phys. Rev.* **181**, 1336 (1969).
- [36] T. J. Scheidemantel, C. Ambrosch-Draxl, T. Thonhauser, J. V. Badding, and J. O. Sofo, Transport coefficients from first-principles calculations, *Phys. Rev. B* **68**, 125210 (2003).
- [37] See Supplemental Material at <http://link.aps.org/supplemental/10.1103/PhysRevB.109.054114> for (1) CRTA calculated transport properties with the fixed structure of the tetragonal phase; (2) electronic band structure and the corresponding DOS for various doping concentrations; (3) Fermi nesting factor for high-symmetry points as a function of doping; and (4) EPC spectral function and transport EPC function for various doping concentrations.
- [38] V. H. Crespi and M. L. Cohen, Possible discrepancies between transport and superconducting electron-phonon coupling due to anisotropic Fermi surface nesting, *Solid State Commun.* **81**, 187 (1992).
- [39] L. Liu, H. Guo, H. Lü, S. Dai, B. Cheng, and Z. Chen, Effects of donor concentration on the electrical properties of Nb-doped BaTiO<sub>3</sub> thin films, *J. Appl. Phys.* **97**, 054102 (2005).
- [40] K. H. Härdtl and R. Wernicke, Lowering the Curie temperature in reduced BaTiO<sub>3</sub>, *Solid State Commun.* **10**, 153 (1972).
- [41] H. Miyazawa, E. Natori, T. Shimoda, H. Kishimoto, F. Ishii, and T. Oguchi, Relationship between lattice deformation and polarization in BaTiO<sub>3</sub>, *Jpn. J. Appl. Phys.* **40**, 5809 (2001).
- [42] A. R. Damodaran, E. Breckenfeld, Z. Chen, S. Lee, and L. W. Martin, Enhancement of ferroelectric Curie temperature in BaTiO<sub>3</sub> films via strain-induced defect dipole alignment, *Adv. Mater.* **26**, 6341 (2014).